Incorporating realistic geophysical effects of mean wind from LIDAR measurements in Large Eddy Simulation of Wind Turbine Arrays

Tanmoy Chatterjee[*], Nihanth Wagmi Cherukuru[†], Yulia Peet[‡], Ronald Calhoun[§]

The present paper aims at performing Large Eddy Simulation of a 3×3 wind turbine array in atmospheric boundary layer, by incorporating realistic large scale geophysical effects, such as the variation in mean wind flux (gusts) and wind direction (wind veer) from the data obtained by field measurements. The purpose of this study is to understand the effect of realistic winds on turbulence and wake interactions, and also on the power generated by the wind turbines. The wind turbines are modelled using a state-of-the-art reduced order actuator line (AL) model, which is computationally more efficient than resolving the blades of the turbine. The inflow conditions are generated by spectrally interpolating the data from a precursor Atmospheric Boundary Layer (ABL) simulation and incorporating the geophysical effects obtained from LIDAR scans to adjust the wind flux and wind direction from the precursor simulations, as appropriate. Additionally, we also present a comparison of the above approach with an LES performed with a standard turbulent inflow to further understand the influence of the geophysical effects on large-scale coherence and subsequently on wind power. Furthermore, the knowledge of the influence of geophysical effects in a long term is expected to improve decision making capabilities in wind farm optimization algorithms and contribute to the design and validation of data assimilation algorithms.

I.   Introduction

Wind turbines, and in particular wind farms have seen a rapid growth in technology since the mid 1980's to meet the ever increasing demands of the renewable energy market. Wind turbines are usually installed in the lower atmospheric boundary layer, and the power generation from the wind turbine is an outcome of a complex interaction of the turbine blades with high *Re* large-scale atmospheric turbulence. Consequently, the design and power optimization of the wind turbines require a careful understanding of the multi-scale dynamics involved in the complex interaction of the wind turbine wakes with an atmospheric boundary layer. This is even more essential in large wind farms, since the reduced velocity wake region from the first row of turbines may impinge on the second row and beyond, thus significantly reducing the wind farm efficiency.[1,2] Numerical simulations, in particular, Large-Eddy Simulations (LES) serve as a cost-effective yet tractable method for studying wind turbine and wind farm turbulence, due to high Reynolds numbers associated with the atmospheric conditions.[3–7] For similar reasons, resolving wind turbine blades with a body fitted mesh is associated with significant costs, especially in a wind farm setting, and hence reduced order Actuator-Line model[8,9] is often employed to model wind turbines in wind farms.

The wake interactions and the power generated by the wind turbines depend significantly on inflow wind conditions.[5,7] Most numerical simulations of wind farms generate turbulent inflow conditions from precursor simulations that assume a constant mean wind speed and wind direction throughout the simulations.

[*]School for Engineering of Matter, Transport and Energy (SEMTE), Arizona State University; E-mail: tchatte3@asu.edu

[†]School for Engineering of Matter, Transport and Energy (SEMTE) , Arizona State University; E-mail: ncherukuru@asu.edu

[‡]Assistant Professor, School for Engineering of Matter, Transport and Energy (SEMTE), Arizona State University; E-mail: ypeet@asu.edu

[§]Associate Professor, School for Engineering of Matter, Transport and Energy (SEMTE), Arizona State University; E-mail: rcalhou@asu.edu

American Institute of Aeronautics and Astronautics

Although the wall-bounded turbulence generated in the precursor is physically consistent in terms of energy cascade and shear stress spectra at different length scales, it differs from realistic wind conditions in its absence of large scale geophysical effects. These effects in general include Coriolis forcing as well as other phenomenon associated with the wind recirculation due to the presence of geographical terrain, variation in wind direction (wind veering), large scale variation in mean wind speeds, and the variation in wind character during the diurnal cycle. The incorporation of the geophysical effects would expectedly generate more realistic winds, and consequently would reveal a different pattern of large scale dynamics, that cannot be seen in a standard turbulent inflow. Consequently, the presence of these geophysical variations would supposedly change the interaction pattern of the turbine wakes in the wind turbine (WT) array compared to the standard turbulent inflow, and hence would alter the power generated by the turbines.

The most accurate representation of the realistic wind conditions would involve a data assimilation[10,11] from field-measurements into the simulations. However, the major challenge in implementing data assimilation in the context of Large Eddy Simulations lies in the disparity of the spatio-temporal resolution of real-time field measurements and the resolution requirement for LES. Both the spatial and temporal resolution of field measurements data (LIDAR scans, in our case) are typically of the order of ~ 100 m and $\sim$ minutes respectively, while for the LES simulation, the resolutions are much smaller, of the order of ~ 10 m and ~ 0.1 sec respectively. To circumvent the resolution mismatch, it is likely that a spatio-temporal interpolation would be required, in addition to already expensive data-assimilation techniques such as 4DVAR[10,12] or iterative Newtonian relaxation,[11] which would create a severe bottleneck in terms of computational cost.

In order to circumvent the issue of computational cost in data assimilation of four dimensional data, in this paper we offer a simpler approach of incorporating some of the geophysical effects into the LES simulations of WT arrays, which involve only a temporal variation, such as the variation of mean wind direction (wind veering) and wind speed due to gusts. These mean winds involve 10-minute temporal averaging of the field data, as well as a spatial averaging normal to the mean flow direction. In this implementation, we only require a temporal interpolation of the mean velocity data onto the LES time scales, which can be implemented with a reasonable computational cost. These mean wind effects will be incorporated in our simulations from the real-time field measurements data using LIDAR scans performed by the Environmental Remote Sensing Group in Arizona State University.[13,14]

In the current paper, we present detailed results of the wind turbine wake interactions, the interaction with the atmospheric turbulence, and the power generated by the turbines, in the presence of a realistic wind inflow incorporating the aforementioned geophysical effects. We also present a detailed analysis that allows us to isolate the effects of the large scale geophysical phenomenon from small-scale effects associated with the boundary layer turbulence, by comparing the LES data with the geophysical effects against a standard constant mean velocity ABL inflow LES computation. This analysis helps to understand how the physics of the large-scale coherence would be changed by the presence of the geophysical phenomenon.

II.   Numerical Method

The numerical method implements a variational formulation of the Navier-Stokes (NS) equations involving Galerkin projection using an open-source spectral element solver **Nek5000**.[15] The domain is partitioned into hexahedral elements in 3D, and within each element any variable can be expanded into a series of orthogonal basis functions (Lagrange-Legendre polynomials) with the grid points clustered towards the element boundaries known as Gauss-Lobato-Legendre (GLL) points, which correspond to the roots of the basis function polynomials. For smooth solutions, exponential convergence can be achieved with increasing the order of the polynomials.

The time discretization of the NS solver in Nek5000 involves third order backward difference scheme, the velocity is solved using preconditioned conjugate gradient (CG) method and the pressure solver uses iterative generalized mean residual solver (GMRES) method in Krylov subspace. The current algorithm was optimized to achieve perfect scalability in parallel implementation for up to 1,000,000 processors.[15]

II.A.   Large Eddy Simulation – Subgrid Closure

The spatially filtered 3D Navier-Stokes equation for LES of wind turbine arrays in neutral ABL flows can be obtained by incorporating a convolution integral filter on the original Navier-Stokes equation as given below. In the LES model, we use a Cartesian coordinate framework, where x is the streamwise direction, y is the

American Institute of Aeronautics and Astronautics

spanwise direction and z is wall normal direction, with $\tilde{u}$, $\tilde{v}$, $\tilde{w}$ being the filtered velocities in x, y, & z directions respectively. In vectorial notation, $\widetilde{\mathbf{u}}$, is the 3D filtered velocity vector, and $\widetilde{p^*}$ is the modified pressure term incorporating the subgrid-scale kinetic energy.

$$\frac{\partial \widetilde{\mathbf{u}}}{\partial t} + \widetilde{\mathbf{u}}\nabla\widetilde{\mathbf{u}} + \frac{1}{\rho}\nabla\widetilde{p^*} - \widetilde{\mathbf{F}} - \nu\nabla^2\widetilde{\mathbf{u}} = -\nabla\cdot\boldsymbol{\tau}(\mathbf{u},\mathbf{u}) \tag{1}$$

The subgrid stress (SGS) tensor in Equation 1, $\boldsymbol{\tau}(\mathbf{u},\mathbf{u}) = \widetilde{\mathbf{u}\mathbf{u}^T} - \widetilde{\mathbf{u}}\widetilde{\mathbf{u}}^T$ arising from the non-commutativity of filtering with the nonlinear advection term, is modelled using a Smagorinsky type eddy viscosity closure. The model SGS stress $\boldsymbol{\tau}^{SGS}(\widetilde{\mathbf{u}},\widetilde{\mathbf{u}})$ can be given as $\boldsymbol{\tau}^{SGS} - \frac{1}{3}tr(\boldsymbol{\tau}^{SGS})\mathbb{I} = -2\nu_t\nabla^s\widetilde{\mathbf{u}}$. In classical Smagorinsky model, $\nu_t = (l_f)^2|\nabla^s\widetilde{\mathbf{u}}|$, with $l_f = C_s\Delta$,[16] Δ is a grid scale and the term $|\nabla^s\widetilde{\mathbf{u}}|$ can be given as $|\nabla^s\widetilde{\mathbf{u}}|^2 = 2\nabla^s\widetilde{\mathbf{u}} : \nabla^s\widetilde{\mathbf{u}}$ and $\nabla^s\widetilde{\mathbf{u}} = \frac{1}{2}(\nabla\widetilde{\mathbf{u}} + \nabla\widetilde{\mathbf{u}}^T)$. For high Reynolds number turbulent ABL flow, we employ the algebraic wall damping by Mason and Thompson (1992),[16]

$$\frac{1}{l_f^n} = \frac{1}{(C_0\Delta)^n} + \frac{1}{\kappa(z+z_0)^n} \quad z_0 \ll H. \tag{2}$$

For best results in our SEM model (see [6] for details), the ad-hoc blending function parameters $C_0 = 0.19$, $n = 0.5$ are used.

II.B. Large Eddy Simulation – Near Wall Modelling

At the bottom surface, we use a wall stress boundary condition without having to resolve the rough wall (cost-prohibitive at such high Re), relating the wall stress vector to the horizontal velocity vector $\widetilde{\mathbf{u}_h}$ at the first grid-point using the standard Monin-Obukhov similarity law[17] along with no-penetration conditions of large eddies, $\widetilde{w} = 0$.

$$\frac{1}{\rho}\boldsymbol{\tau}_s = -\kappa^2 \frac{\widehat{\widetilde{\boldsymbol{u}}}_{h,\frac{\Delta z}{2}}(x,y,t)|\,\widehat{\widetilde{\boldsymbol{u}}}_{h,\frac{\Delta z}{2}}|(x,y,t)}{\log\left(\frac{z}{z_0}\right)\Big|_{\frac{\Delta z}{2}}^2} \tag{3}$$

where, $\left|\widehat{\widetilde{\boldsymbol{u}}}_{h,\frac{\Delta z}{2}}\right| = \sqrt{\widehat{\widetilde{u}}_{\frac{\Delta z}{2}}^2 + \widehat{\widetilde{v}}_{\frac{\Delta z}{2}}^2}$ and $\widehat{\widetilde{\boldsymbol{u}}}_{h,\frac{\Delta z}{2}} = \widehat{\widetilde{u}}_{\frac{\Delta z}{2}}\vec{e_x} + \widehat{\widetilde{v}}_{\frac{\Delta z}{2}}\vec{e_y}$ ($\vec{e_x}, \vec{e_y}$ are unit vectors in the x, y direction). The "hat" represents additional explicit filtering carried out in the modal space by attenuating $k_c = 4$, highest Legendre polynomial modes of the spectral element model.[6] For collocated spectral element methods $\widehat{\widetilde{u}}_{\frac{\Delta z}{2}}$, $\widehat{\widetilde{v}}_{\frac{\Delta z}{2}}$ are calculated as an interpolation at half wall node $\Delta z/2$ e.g., between $\widehat{\widetilde{u}}(x,y,0,t)$ and $\widehat{\widetilde{u}}(x,y,z=\Delta z,t)$ (and similar procedure for $\widehat{\widetilde{v}}$) and $\Delta z/z_0 \gg 1$, where z_0 is the aerodynamic bottom-wall roughness.

II.C. Actuator Line Model: Turbine Response

In an actuator line model,[9] the blades of aerofoil cross section are divided into elements, similar to the Blade Element Momentum Theory (BEM), and the local lift (L) and drag (D) force experienced by each element is calculated as $(L \,,\; D) = \frac{1}{2}C_{(l,d)}(\alpha)\,\rho\,V_{rel}^2\,c\,w_d$, where c, w_d are chord-length and blade width respectively. The lift and drag coefficients, C_l, C_d of the aerofoil are computed beforehand from DNS or wind-tunnel experiments. In the current paper, C_l, C_d were taken from standard NACA airfoil look-up tables and no 3D or stall corrections were implemented. The local aerodynamic force $\vec{f} = L\vec{e_L} + D\vec{e_D}$ (here $\vec{e_L}$ and $\vec{e_D}$ are the unit vectors in the direction of the local lift and drag, respectively) can be calculated by computing the angle of attack, α from the relative velocity, V_{rel}, streamwise velocity, V_x and the pitch angle, γ (Figure 1). The total reaction force from all the blade elements experienced by the fluid distributed smoothly on several mesh points is given by

$$\vec{F}(x,\,y,\,z,\,t) = -\sum_{i=1}^{N}\vec{f}(x_i,\,y_i,\,z_i,\,t)\,\eta_\epsilon(|\vec{r}-\vec{r_i}|), \tag{4}$$

using a smeared out delta function in the form of a Gaussian $\eta_\epsilon(d) = 1/\epsilon^3\pi^{3/2}\exp\left[-\left(d/\epsilon\right)^2\right]$. The summation in the forces is over all N blade elements, and $\epsilon = 2\,w_d$ is used in the current study for optimum results. The AL model is more advanced than the actuator-disc model[18] commonly used in numerical computations of periodic wind farms, in its capability to capture the tip-vortices being shed in the near-wake quite accurately.[6,9]
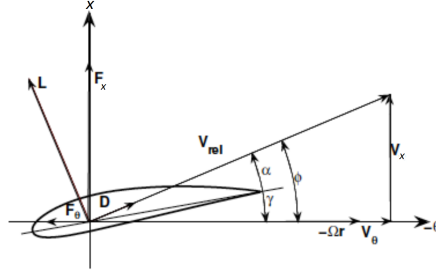
American Institute of Aeronautics and Astronautics

Figure 1: Velocity triangle for the determination of the local relative velocity on a turbine blade.

III. Computational Setup

III.A. Precursor Simulation – Atmospheric Boundary layer

The computational domain of the precursor ABL simulation is of rectangular geometry and Cartesian spectral element collocated mesh has been used for such calculations. In the present Cartesian framework, x is the streamwise direction, y is the spanwise direction and z is wall normal direction, with $\tilde{u}$, $\tilde{v}$, $\tilde{w}$ being the filtered velocities in x, y, & z directions respectively. We model a similar setup as in Ref. [19] for neutrally-stratified ABL simulations with periodic boundary conditions in the streamwise spanwise direction. The bottom-wall shear stress boundary conditions are given in Section II.B, while the top boundary conditions are stress-free: $d\tilde{u}/dz = d\tilde{v}/dz = \tilde{w} = 0$. The computational domain for the ABL simulations is $2\pi H \times \pi H \times H$, where $L_x = 2\pi H$, $L_y = \pi H$, and $L_z = H$ is the boundary-layer thickness as in Ref. [6,7]. The domain is uniformly discretized into $30 \times 20 \times 24$ elements in $x, y,$ and z directions respectively. With 8^3 GLL points per element, the number of grid points for the ABL simulations is $211 \times 141 \times 169 \approx 5 \times 10^6$ (For more details of the simulation parameters, see [7]). In the standard neutral ABL precursor, we incorporate the driving streamwise force (pressure gradient) which maintains a bulk mean velocity by using splitting scheme (solving the unsteady Stokes equation)[20] in the NS equation.

Figure 2 shows a very good trend of the streamwise mean velocity gradient, especially in the log-layer ($z/H \leq 0.1$) with our robust and well designed spectral element LES model of neutrally-stratified atmospheric boundary layer simulation.[21] The lower 10% of the inner layer, $z/H \leq 0.1$, should exhibit the log-law of the wall, manifesting $\phi(z) = 1$. Both the state-of-the-art Lagrangian averaged scale dependent dynamic Smagorisky model,[22] as well as our best tuned wall-damped standard Smagorinksy closure, shows excellent trends of the log-layer.[23]
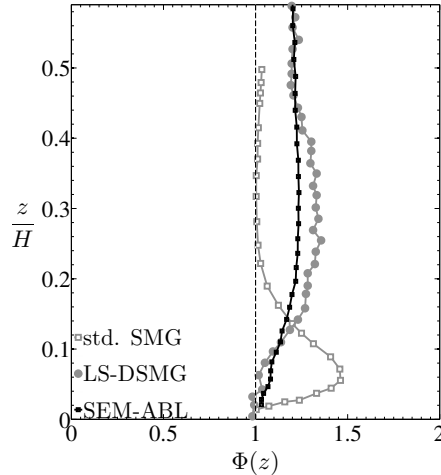

Figure 2: Temporally and horizontally averaged mean streamwise velocity gradient $\phi = \kappa z/u_\tau d\bar{U}/dz$ vs normalized height z/H. LS-DSMG is state-of-the-art Lagrangian averaged scale dependent dynamic Smagorinsky model for LES closure,[22] and std. SMG is the standard Smagorinsky model for LES closure.[22] SEM-ABL: – spectral element simulation with best results: Wall damped standard Smagorinsky closure.[16]

American Institute of Aeronautics and Astronautics

III.B.   A Splitting Scheme for Incorporation of Geophysical Effects

Incorporating the geophysical effect of the varying mean wind speed is implemented by changing the pressure gradient forcing accordingly through the Stokes solver in the preprocessor step.

The Navier-Stokes (NS) equation in the operator form can be given as

$$\mathfrak{L}_1(\mathbf{u}) + \mathfrak{L}_2(p) = \mathfrak{NL}(\mathbf{u}, \nabla\mathbf{u}) + \mathbf{f} + B.C. \tag{5}$$

where the linear operators, $\mathfrak{L}_1 = \partial/\partial t - (\nu + \nu_t)\nabla^2$, $\mathfrak{L}_2 = 1/\rho\nabla$, and the non-linear operator $\mathfrak{NL}(\mathbf{u}, \nabla\mathbf{u})$ have been used as a compact notation for the corresponding NS operators. In this analysis, the NS equations involved are in the LES framework, and hence the tilde $\sim$ have been dropped from all the terms for brevity. ν is the kinematic viscosity of the fluid, while ν_t is the LES filtering eddy viscosity based on Smagorinsky type of closure. The splitting scheme for the NS equation (Equation 5) can be given as follows.

$$\mathfrak{L}_1(\mathbf{u}') + \mathfrak{L}_2(p') = \mathfrak{NL}(\mathbf{u}', \nabla\mathbf{u}') + \mathbf{f}_a + B.C. \tag{6}$$
$$\mathfrak{L}_1(\mathbf{u}_0) + \mathfrak{L}_2(p_0) = \mathbf{f}_0 + B.C.(0) \tag{7}$$

The forcing function $\mathbf{f}_a$ corresponds to the time-dependent actuator line forcing, while $\mathbf{f}_0$ represents the time-invariant pressure gradient forcing of the homogeneous linear NS equation. BC in Equation 6 is the boundary condition for the 3D inhomogeneous problem, with the inflow boundary conditions taken as a time-dependent instance of a turbulent flow realization from precursor simulations at a specified flow cross-section spectrally interpolated onto the wind turbine array grid, while the boundary conditions in wall-normal and spanwise directions correspond to those of the precursor as documented in Section III.A. The homogeneous boundary condition $BC(0)$ for the linearized split NS equation (Equation 7), comprises of periodic boundary conditions in the streamwise, spanwise direction, while homogeneous Neumann type stress-free boundary conditions are implemented in the wall-normal direction.

The reconstruction of the total NS velocity, forcing and pressure variable from the splitting terms can be obtained as

$$\begin{aligned} \mathbf{u} &= \mathbf{u}' + \alpha\mathbf{u}_0 \\ p &= p' + \alpha p_0 \\ \mathbf{f} &= \mathbf{f}_a + \alpha\mathbf{f}_0 \end{aligned} \tag{8}$$

α being a free parameter, which can be calculated at each time step from the specified flow rate constraint at that particular time. With flow-rate at time t, being $c(t)$, and A and V being the cross-sectional area of the flow and computational volume of the domain respectively, the flow rate can be written as

$$c(t) = \frac{A}{V}\int_\Omega \mathbf{u}\,\mathrm{d}\Omega = \frac{A}{V}\int_\Omega (\mathbf{u}' + \alpha\mathbf{u}_0)\,\mathrm{d}\Omega \tag{9}$$

Consequently,

$$\alpha(t) = \frac{\left(c(t) - \frac{A}{V}\int_\Omega \mathbf{u}'\,\mathrm{d}\Omega\right)}{\frac{A}{V}\int_\Omega \mathbf{u}_0\,\mathrm{d}\Omega} \tag{10}$$

The algorithm thus proceeds as follows. Equation 7 is solved once at the preprocessor step and its solution is stored in memory. At each subsequent time steps, Equation 6 is solved with the time-dependent actuator line forcing $\mathbf{f}_a$ and time-dependent inflow conditions from precursor. The resulting solution corresponding to a specified flow rate $c(t)$ calculated from LIDAR scans as described below is then obtained from Equations 10 and 8 at each time t without any iteration.

The variation in the wind direction (wind veering – geophysical effect) can also be incorporated quite easily during the spectral interpolation of the inflow condition using stationary overlapping mesh methodology.[24] Ideally, variation in the wind direction should be incorporated by rotating the whole precursor simulation domain; however, since variation of wind direction from LIDAR scans is within $\pm 6°$ (See Figure 4d), we rotate only the inflow vector (u, v velocities) instead of rotating the whole precursor domain. This allows us to save significantly on the computational cost that would be associated with remeshing and interpolation at every timestep, in the setting of the moving domain of the precursor simulation. Equation 11 shows

American Institute of Aeronautics and Astronautics

the horizontal inlet velocities u_{inlet}, v_{inlet} obtained from horizontal velocities u, v of precursor ABL in the midplane, $x = \pi H$, with the mean wind direction θ_{mean}.

$$
\begin{aligned}
u_{inlet} &= u\cos(\theta_{mean}) + v\sin(\theta_{mean}) \\
w_{inlet} &= -u\sin(\theta_{mean}) + v\cos(\theta_{mean})
\end{aligned}
\tag{11}
$$

Here θ_{mean} in Equation 11 is calculated first by subtracting dominant mean direction of the flow, from the mean wind direction in Figure 4b, and finally subtracting it from $180°$ to be compatible with current Cartesian framework.

III.C. Obtaining real-time Geophysical Flow Parameters from LIDAR scans

III.C.1. Field Measurements of data using LIDAR

Lidars (Light Detection and Ranging) are becoming increasingly favoured in the atmospheric science[14] as well as in the wind energy community,[13,25] because of its ability to collect field data for a massive spatial extent of tens of kilometers, and very accurate terrain mapping of complex topographies. The Doppler lidar (Lockheed Marteen Coherent Technologies) at Environmental Remote Sensing Group at Arizona State University was employed to collect wind data from Tehachapi pass, California. The lidar was deployed on the Windland, Inc. wind farm which is on a ridge (1450 m above sea level) at the northwest part of the Tehachapi wind farms. However, only the upstream location of the wind farms has been scanned, to collect radial velocity data from the ridge location, emulating atmospheric boundary flows. Figure 3 shows the scanning region of the doppler lidar in the Tehachapi ridge, which is a relatively flat location, surrounded by a complex terrain, and satisfying approximate neutral ABL conditions over the computational time.

III.C.2. Resolution of Lidar Scan

The WindTracer Lidar deployed in the Tehachapi ridge, has a wavelength of 1.6 μm and pulse repetition frequency of 750 Hz, with each pulse containing about 2 mJ of energy. The lidar has a scanning range from 400m - 10 km (depending on atmospheric conditions), with a spatial resolution of 100m, and a temporal resolution of $25 - 30$ secs. The radial velocity resolution of the scans are range dependent, varying from 0.5 - 1 m/s with a range of 38 m/s. The maximum height achievable by the lidar pulses vary from 2 - 4km, dependent on atmospheric conditions. In the Tehachapi ridge location, a stack of PPI (Plan Position Indicator- only varying azimuth) scans at varying elevation has been performed to collect the radial velocity data. Using the velocity retrieval algorithm, time varying 2D cartesian vector fields were obtained on a $6km \times 4km$ rectangular domain ($\sim xy$ plane of ABL domain) with a spatial resolution of 100m and a temporal resolution of 25s. The raw lidar data was initially quality controlled based on a simple SNR based filter, i.e., points with very high SNR (indicative of hard target returns) and very low SNR (dominated by noise) are rejected. However, the accuracy of the Lidar data degrades significantly with increasing height of the PPI stacks. Moreover, in Lidar scans, velocity retrieval algorithm assumes, 2D planar velocities, along the plane of the PPI stacks, which also degrades the divergence free constraint of the flow. In the next section, we discuss the coupling of the Lidar data in LES simulation, with certain wall-bounded turbulence assumption, that supposedly does not degrade the accuracy of the data.

III.C.3. Data Coupling

The LIDAR scanned field data and the LES simulations differ substantially in the spatial and temporal scales of resolution. For ABL thickness, $H = 1000m$, the spatial resolution of field measurements is $\sim 100m$, while that for LES simulation is $\sim 25m$. The disparity in the temporal resolution is even bigger, with field measurements having data at 25 secs interval for a span of 3 days, while the timesteps in LES are much stringent, ~ 0.1 seconds, and has a capability of running on a scale of hours for a reasonable computational cost. In our current simulation, however, we can circumvent the disparity in the spatial resolution, since we incorporate information of the bulk mean speed, through spatial averaging (cross-section of the flow). The temporally varying wind speed, is filtered through a 10-minute averaging, which removes the small scale turbulent noise, retaining only the large scale coherent variation of the mean with time. The spatial averaging of the velocity is done as follows. We consider a PPI-stack, in the near wall log-layer region, with a dominant velocity in the streamwise direction (or more appropriately in the direction of the line-of-sight of

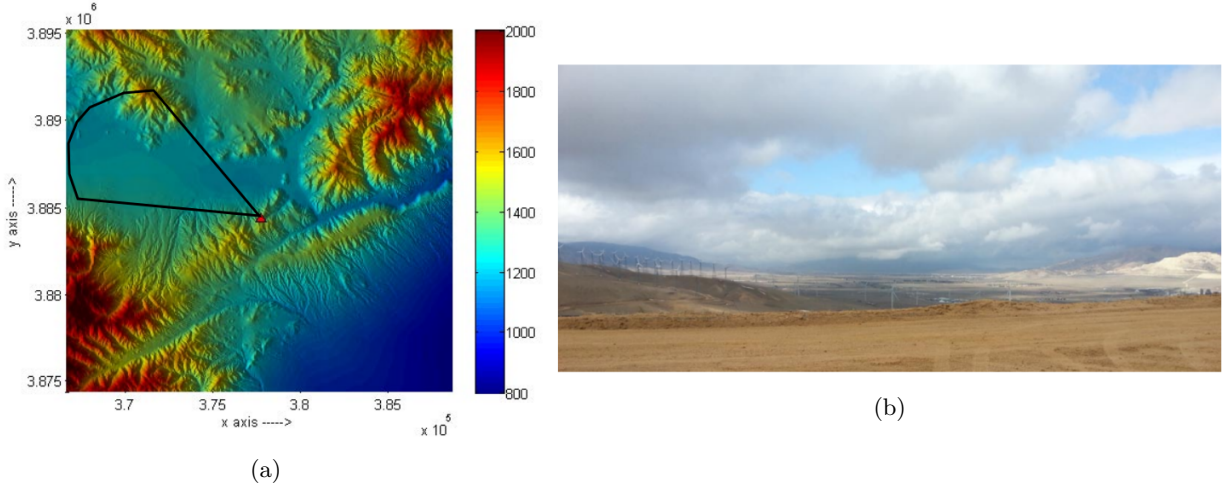American Institute of Aeronautics and Astronautics

Figure 3: (a) Tehachapi topography around the lidar, with height measured in meters. The lidar location is identified by the red triangle; the black radial sector denotes the scanning region of the lidar (b) Photo of view to the northwest of Tehachapi pass, where the upstream scan is performed, from the lidar location. Image courtesy: Masters Thesis of Beth Magerman, ASU.[26]

the lidar pulse), and then averaging across a line orthogonal to the direction of the flow. We further assume a log-law fit of the streamwise velocity with height, with the velocity information only from that PPI-stack, and subsequently integrating over the wall-normal direction, we can retrieve, the spatially averaged mean wind speed, with a reasonable accuracy. In an analogous way considering the 10 minute and the line (orthogonal to the dominant direction of flow) averaged horizontal velocities, we can also retrieve, the variation of the mean wind direction (wind veer) in a straightforward manner.

Table 1 shows an estimation of real-time of data that can be collected in precursor (ABL) and WT array simulations based on a reasonable computational cost (CPU-hours). This clearly indicates that the simulation capabilities of the precursor simulation and WT array in real-time are limited to the time-scale of hours. Figures 4a, 4b shows the data obtained corresponding to the variable bulk mean wind speed (variable flux) and wind direction collected for over 2 days, and the window scale of hours over which the simulation is completed. Specifically, we select a 4 hour window-frame (Figure 4c), where a strong variation of the bulk mean wind speed is observed (in a time-scale of minutes – resolvable by LES) reminiscent of sudden gusts. We incorporate this mean wind speed by implementing the time-dependent flow rate through the linear Stokes-operator as in splitting scheme (See Section III.B). Analogous to the mean wind, the wind direction in the $\sim$ 4 hour window frame (Figure 4d) is also incorporated during the spectral interpolation of the inflow condition. The blue-circles in Figures 4a, 4b indicate the time locations in the simulations for which the instantaneous velocity snapshots are presented, containing a significant variation of mean wind flux, but not wind direction. We also present the spectral information of the mean wind and wind direction at various temporal scales (involving the Fourier transform) in Figure 4e.

Case	Timestep (sec)	Flow-through time	Real Time (hrs)	CPU-hours
ABL	0.1	52	4	0.05M
WT	0.08	35	4	0.25M

Table 1: Temporal simulation parameters of ABL and WT array based on 15 m/s winds.

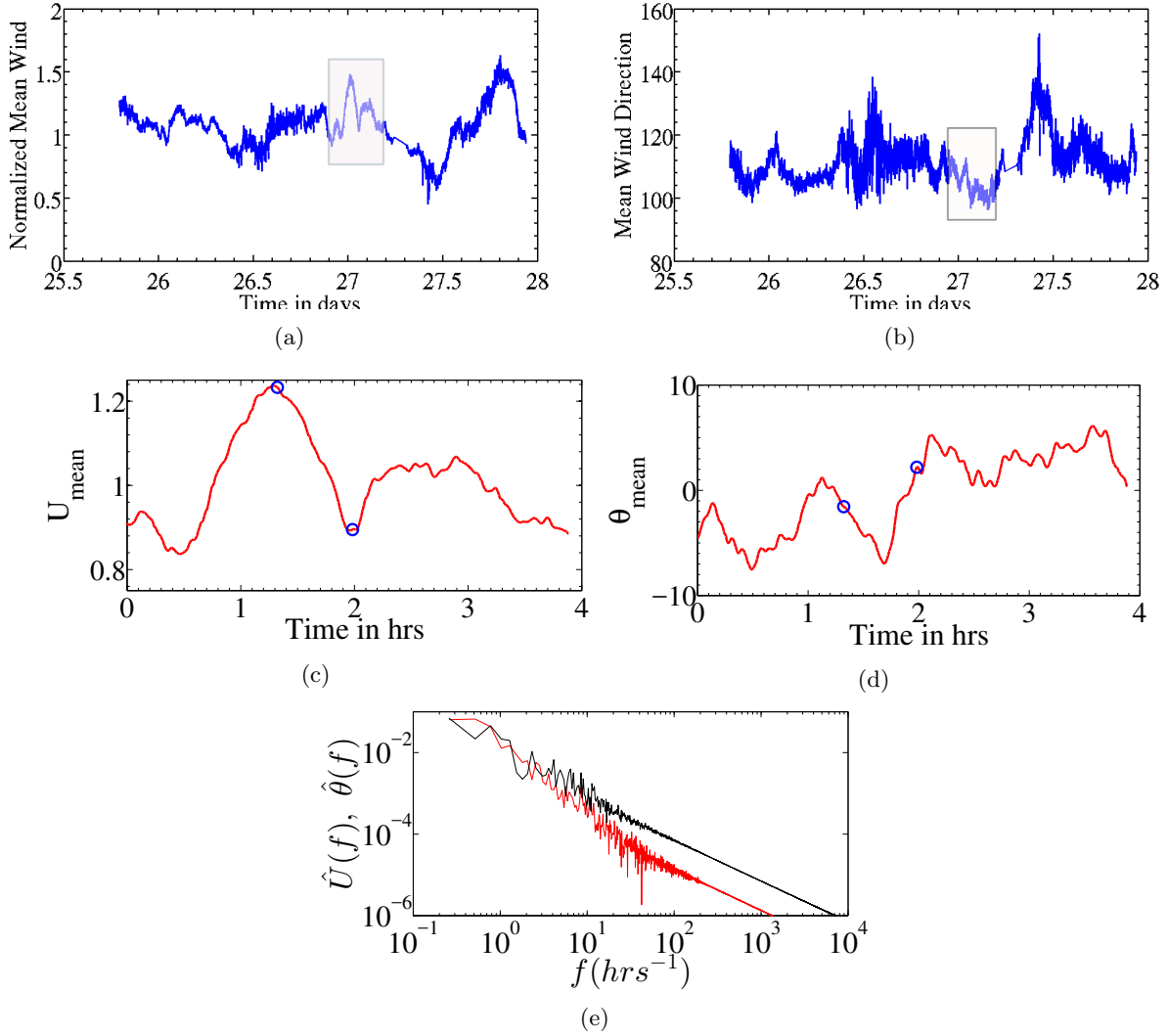American Institute of Aeronautics and Astronautics

Figure 4: Temporal variation of mean wind speed and wind direction obtained from LIDAR scan. Mean obtained from 10-minute temporal averaging & averaging through the flow-cross section area. (a), (b) Mean wind speed and direction over a span of 3 days. (c), (d) Mean wind speed and direction over the zoomed window of ∼4 hours as shown in Figure (a), (b). Blue curve ((a),(b)) – true temporal variation. Red curve ((c), (d)) – gaussian filtered variation. Blue circles in (c), (d) are the time-locations 1 hour 20 minutes and 1 hr 59 mins of the simulation. (e) Fourier spectrum of the mean wind $\hat{U}(f)$ (black) and wind direction $\hat{\theta}(f)$ (red) for the windowed data in our simulation.

III.D. LES-AL Simulation of Wind Turbine Array

The domain size for the 3×3 wind turbine array is $3\pi H \times \pi H \times H$, with the statistically stationary ABL simulation serving as an initial condition to the turbine array domain. Consequently, a separate ABL simulation at that domain length has been run with a uniform discretization of $40 \times 20 \times 24$ elements to generate realistic initial conditions for turbine array simulations. The details of the grid-requirements of the precursor ABL and the WT array can be found in Table 2. The domain size rescaled in terms of the turbine rotor diameter is given as $47D \times 16D \times 5D$, where $D = 0.2H$ is the diameter of each turbine-rotor. The hub-height of all the turbines are at $z_h = D$. The 9 turbine rotors have been arranged in a 3×3 matrix arrangement in the computational domain. The first row of 3 rotors are placed at $\pi H/2$ or $8D$ distance from the inflow boundary. The streamwise distance between the turbines is $7D$, while the spanwise distance is $3D$. The design of the computational domain and the arrangement of different turbines are done

American Institute of Aeronautics and Astronautics

Case	Geometry	$N_x^e \times N_y^e \times N_z^e$	Grid points
ABL	$2\pi H \times \pi H \times H$	$30 \times 24 \times 20$	5.03×10^6
WT array	$3\pi H \times \pi H \times H$	$48 \times 24 \times 26$	1.04×10^7

Table 2: Computational domain and grid-requirements for ABL & wind turbine array computational domain. 8 GLL nodes has been used per cartesian direction

in concordance with the experimental set up as in Ref. 27 (See Figure 5). The 3×3 array is in essence, a finite-length scale wind farm,[5] and consequently would manifest many complex realistic phenomenon like inner layer growth, turbine wake impingements in second row and beyond, unlike the massive wind farms which are often modelled with streamwise periodic boundary conditions (See Wind Turbine Array Boundary Layer [18, 23, 28]). The details of the grid-design as well as the simulation parameters of the 3×3 array can be found in Ref. 7.
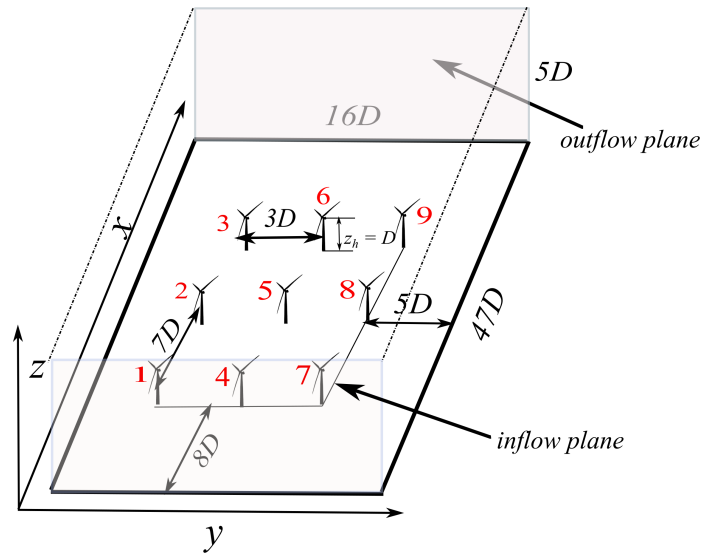

Figure 5: Computational domain of Wind Turbine Array simulations with inflow-outflow condition. Numbers 1–9 in red indicate the turbine number.
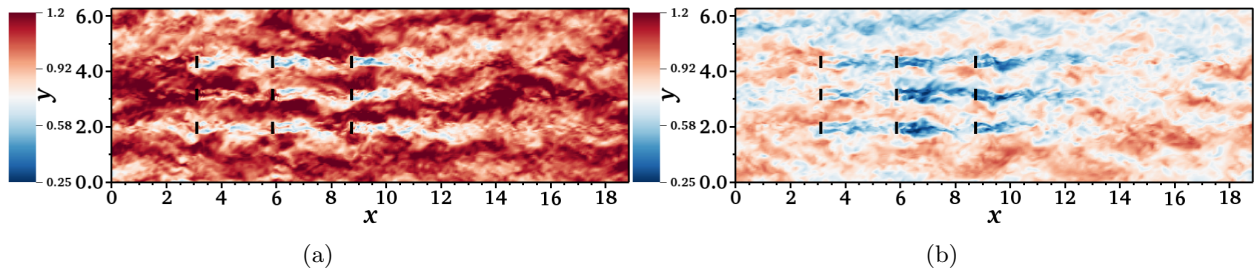

Figure 6: xy snapshots ($z = 0.2H$ from bottom wall) of the instantaneous streamwise velocity u normalized by bulk mean velocity U_m averaged over the time range of data collection, for different times (a) 1hr 20 mins (b) 1 hr 59 mins. Thick solid black lines – turbine positions.
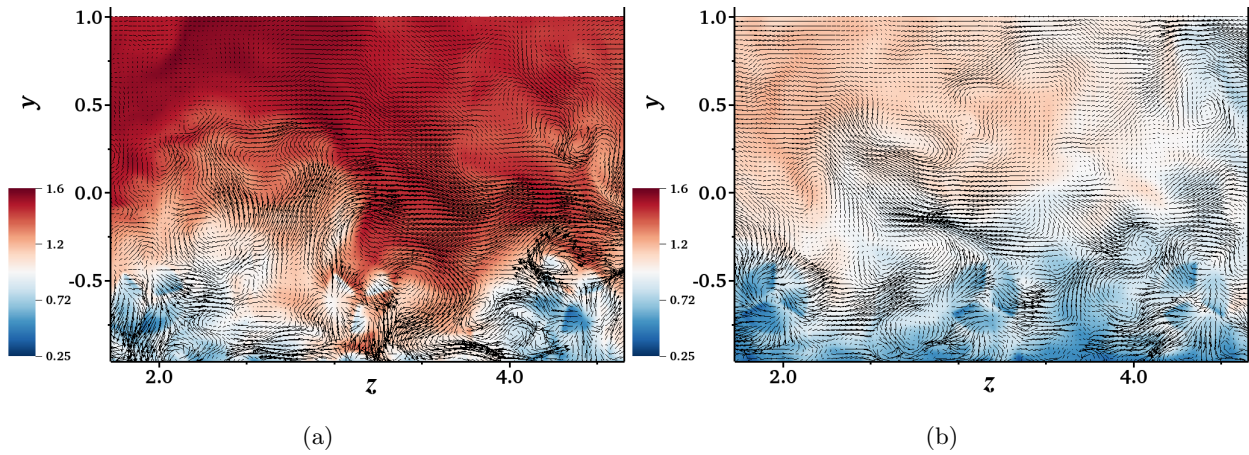
American Institute of Aeronautics and Astronautics

Figure 7: yz snapshots ($x = \pi H$) of the instantaneous streamwise velocity u normalized by bulk mean velocity U_m averaged over the time range of data collection, for different times (a) 1hr 20 mins (b) 1 hr 59 mins. Vectors represent in-plane v, w velocities.
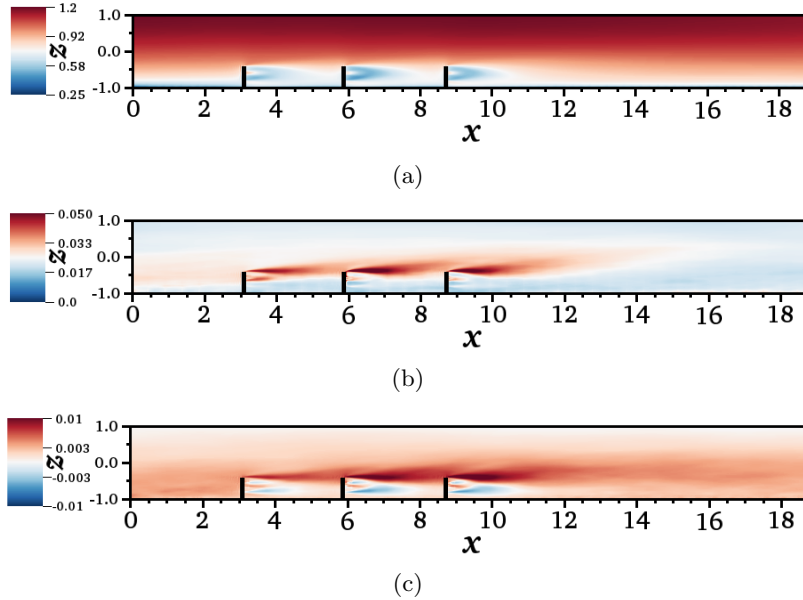

Figure 8: xz plane ($y = \pi H$) of (a) mean streamwise velocity $\overline{U}/U_m$ (b) rms of the streamwise fluctuating component $\overline{u'^2}/U_m^2$ (c) kinematic shear stress $\overline{u'w'}/U_m^2$. Temporal average performed over the time of computation ~ 4 hrs.
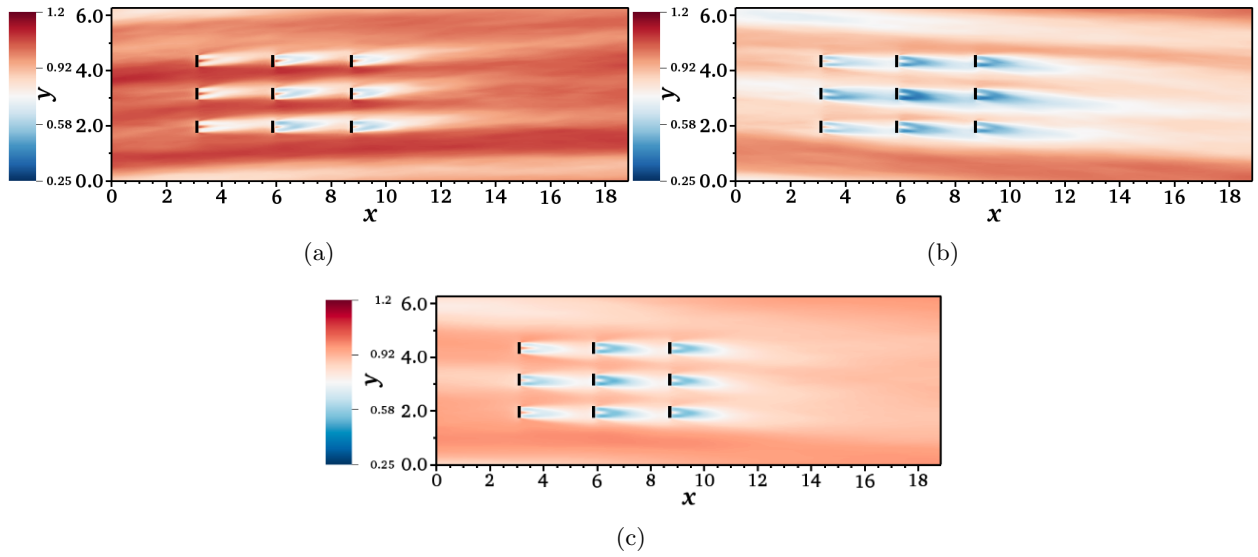
American Institute of Aeronautics and Astronautics

Figure 9: xy plane of temporally filtered normalized mean streamwise velocity $\widetilde{U}/U_m$. $\sim$: temporal filtering over 1.5 flow-through times or 10 mins span. (a) 1 hr 24 mins – 1 hr 34 mins (b) 2hr 9 mins – 2hr 19 mins. (c) Temporally averaged streamwise velocity $\overline{U}/U_m$, averaged over the computational time.

IV.   Results & Discussion

In this section the instantaneous as well as mean and turbulent statistics of the wind flow past the turbine array along with the spectral analysis of the wind turbine power has been discussed in details. The computational simulation has been performed for a span of 4 hrs. The time window of the simulation extends from 0 to 4 hrs and the occurrence of an event at x hrs means x hours from the start of the simulation. The analysis of turbine power has been further extended to incorporate the comparison of results without the variable mean and variable direction of the wind as in Ref. 7.

Figure 6 manifests the xy snapshots of the flow past the wind turbine array at two different times within the 4 hour computational span. The variation of the wind direction is reflected in the dynamically changing yawed turbines, while variable mass flux (mean wind) in the flow is manifested by the variation of color-patch of the over-all velocity in the whole domain at different times.

The snapshot of the flow-structures in the first row of turbines (yz plane) are illustrated in Figures 7a, 7b. Apart from the multiscale flow structures observed around the turbines, the vector plots also indicate the presence of yz circulations of scale $\sim D$ around and above the turbines which are the potential signatures of the large scale structures $\gg O(D)$ possibly contributing to the wind turbine power.[23]

The temporally averaged mean and turbulent statistics of the flow are shown in Figures 8a, 8b and 8c. While not so conspicuous in the mean streamwise velocity $\overline{U}$, the rms of streamwise turbulent fluctuating velocity $\overline{u'^2}$ (u contribution of turbulent kinetic energy), and the kinematic shear $\overline{u'w'}$ prominently display the growth of the inner layer in the presence of variable mean flux and wind direction, similar to what observed in Ref. 7. Figure 9 shows the temporally filtered streamwise velocity $\tilde{U}$, filtered over 1.5 flow-through times. Flow-through time is defined as time-scale L_x/U_m, where L_x is the length of the streamwise domain and U_m is the temporal average of the mean wind flux over the whole computational time. The temporally filtered xy plots at $z = 0.2H$ (hub-height) from the "wall" prominently show the effect of dynamically varying yawed turbines at two different time snapshots.

IV.A.   Power Analysis

In this section we discuss the power generated by the wind turbines and also present some additional spectral analysis of the temporal power signals. The power generated by the turbine t_i at time t is represented as $\mathfrak{P}_{t_i}(t)$. The power generated by the wind turbines are plotted as modified power cofficients of turbine t_i

American Institute of Aeronautics and Astronautics

which are defined as

$$C_p(t) = \frac{\mathfrak{P}_{t_i}(t)}{\frac{1}{2}\rho U_m^3 A_{rot}} \qquad (12)$$

where U_m is the temporal average (over 4 hrs) of the mean wind flux and $A_{rot} = \pi(R_o^2 - R_i^2)$ is the effective rotor area intercepted by the wind. Here, R_o is the rotor radius and R_i is the hub radius.

The power generated by the different turbines at various times are depicted in Figures 10a, 10b and the
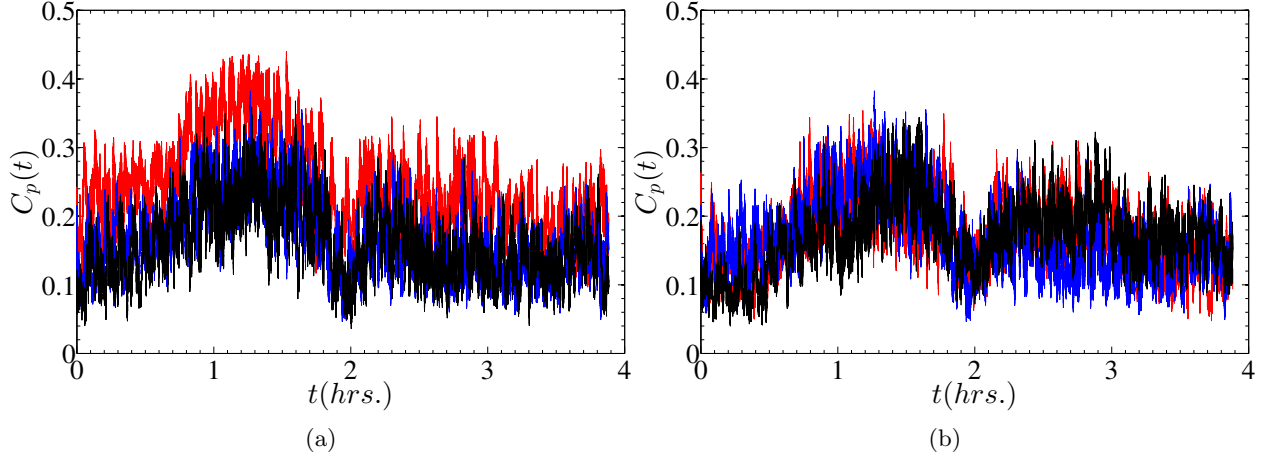

(a)

(b)

Figure 10: Temporal variation of power along different rows and columns in the array. (a) Different row: Red – turbine 4; Blue – turbine 5; Black – turbine 6 (b) Different column: Red – turbine 2; Blue – 5; Black – turbine 8.

.

mean power in each turbine is documented in Table 3. The table not only documents a consistent drop in power from the second and third row as opposed to the first row of turbines due to wake impingement effects, but also depicts some variability ($\sim 2\%$) of power among different columns attributed to the combined effect of yawing due to wind veer and the *locking* of large scale structures due to periodic boundary conditions in precursor simulation.[29] A locking of large scale structures (See Ref. 29 for details), which is a numerical artefact, can be observed, for example, in the banded structures in the spanwise (yz) plane contour of the temporally averaged streamwise velocity (Figure 9c). It will be shown later that locking effects have much smaller influence on power variability compared to the geophysical effects, by comparing with the case of a standard turbulent inflow in Figure 11.

Figures 10a, 10b indicate that the effect of wake-impingements of the second and third row of turbines resulting in a drop of power as opposed to the first row is observed consistently at all times of the flow, while power along the different columns of the turbines do not vary as significantly as in the rows. For completeness of the discussion, we compare the results of the mean power across different rows of the turbines for standard turbulent inflow[7] as well as the turbulent inflow with the geophysical effects in Figures 11. They clearly indicate that the geophysical effects, not only does reduce the wake-impingement effects slightly ($\sim 15\%$ improvement in power from the second/third row), but also increases the variation of mean power along the columns, possibly due to changing mean wind direction. Additionally the power plots in Figure 11a indicate that the spanwise variations due to the "locking of physical structures" are minimal. Furthermore, the large time-scale variation of power is also noted in accordance with the large scale geophysical variations as in Figure 4 which are further analyzed in the spectral space.

Cross-correlation spectra of two power signals $\mathfrak{P}_{t_i}(t)$, $\mathfrak{P}_{t_i}(t)$ is given by

$$P_{t_i t_j}(f) = \int_{-\infty}^{\infty} R_{t_i t_j}(\tau)e^{-2\pi i f \tau}\mathrm{d}\tau \qquad (13)$$

where the cross-correlation of "stationary" power signals $R_{t_i t_j}(\tau = t - t')$ is illustrated below. For $i = j$, we obtain the auto-correlation of the temporal signal $\mathfrak{P}_{t_i}$

$$R_{t_i t_j}(t - t') = \langle \mathfrak{P}_{t_i}(t)\mathfrak{P}_{t_j}(t') \rangle \qquad (14)$$

R \ C	C1	C2	C3
R1	T1 - 0.2673	T4 - 0.2448	T7 - 0.2531
R2	T2 - 0.1763	T5 - 0.1692	T8 - 0.1719
R3	T3 - 0.1586	T6 - 0.1605	T9 - 0.1594

Table 3: Mean modified power coefficient C_p along with the turbine number for different turbines. R_i, C_j represents the ith row and j^{th} column; T_n, $n = 1 \ldots 9$ is the turbine index (See Figure 5).
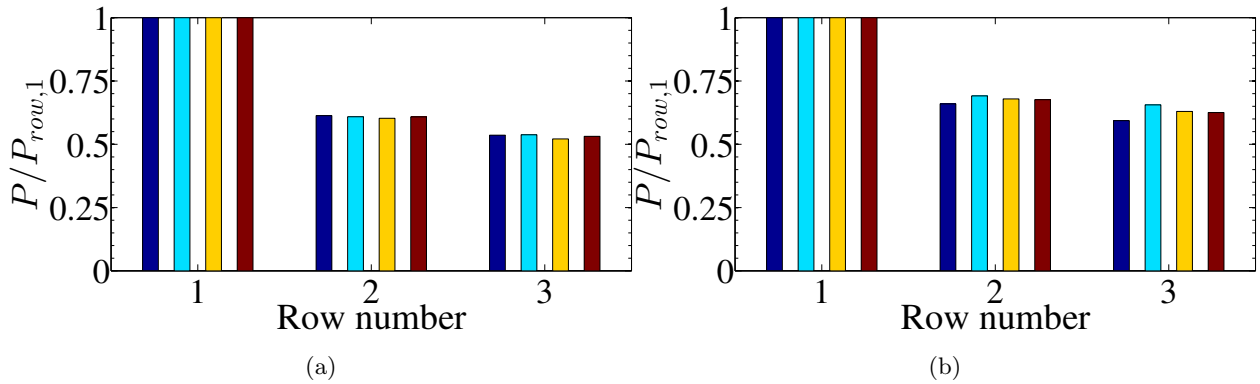
(a)

(b)

Figure 11: Power variation across turbines in different rows in (a) standard turbulent inflow[7] (b) turbulent inflow with geophysical variations. Power is normalized by the turbine power in the first row. Blue – column 1; Cyan – Column 2; Yellow – Column 3; Brown – Column averaged.

In our current computations the cross-correlation and the autocorrelation spectra (also known as the Power Spectral Density (PSD)) are calculated in the discrete sense and the algorithmic approach is provided below. For the discrete time signal $\mathfrak{P}_t$ of size N, the discrete Fourier transform is performed in Equation 15.

$$\hat{\mathfrak{P}}_{tk} = \sum_{j=0}^{N} \mathfrak{P}_t e^{(-2\pi ijk/N)} \tag{15}$$

Consequently the discrete PSD can be obtained from the Fourier coefficients as

$$
\begin{aligned}
P_0 &= \frac{1}{N^2} |\hat{\mathfrak{P}}_{t0}|^2 \\
P_k &= \frac{1}{N^2} [|\hat{\mathfrak{P}}_{tk}|^2 + |\hat{\mathfrak{P}}_{tN-k}|^2] \\
P_N &= \frac{1}{N^2} |\hat{\mathfrak{P}}_{tN/2}|^2
\end{aligned}
\tag{16}
$$

As the sample size N approaches infinity, the continuous framework of the power spectral density can be recovered as well,

$$\lim_{N \to \infty} P_k \to P_{t_i t_i}(f). \tag{17}$$

For brevity, we define the spectral coherence of two temporal signals $\mathfrak{P}_{t_i}(t)$, $\mathfrak{P}_{t_j}(t)$ in the continuous framework, with $P_{t_i t_i}(f)$ being the power spectral density of the power of turbine t_i and the cross spectral density of $|P_{t_i t_j}(f)|^2$ involving turbines t_i, t_j,

$$
\begin{aligned}
C_{t_i t_j}(f) &= \frac{|P_{t_i t_j}(f)|^2}{P_{t_i t_i}(f) P_{t_j t_j}(f)} \\
\phi_{t_i t_j}(f) &= \arg(P_{t_i t_j}(f)).
\end{aligned}
\tag{18}
$$

American Institute of Aeronautics and Astronautics

Here $C_{t_i t_j}(f)$ is the magnitude of the spectral coherence and $\phi_{t_i t_j}(f)$ indicates the phase of the spectral coherence. The spectral coherence of the two temporal signals as described above is an efficient measure of the correlation of two signals at different spectral (frequency) scales of the flow. Analogous to the discrete PSD the discrete cross-correlation spectra are also calculated in a similar fashion as in Equation 16.

V. Conclusions

In the current paper we present the results of wind turbine simulations at $Re \sim 10^{10}$, using realistic inflow boundary conditions with the geophysical effects of mean wind. The results indicate that the large scale geophysical effects (variable mean wind flux, variable mean wind direction) decrease the wake impingements (better power recovery in the second and third rows) slightly but does not influence important flow features like the growth of the inner layer, and -1, $-5/3$ law of the power spectra corresponding to intermediate time scales when compared with the standard turbulent inflow case. A thorough understanding of the power generation by the wind turbines due to the geophysical effects are also provided in the present paper using power spectral density of the turbine power as well as spectral coherence of temporal power signals from the different turbines. These results indicate that in large time scales the influence of these geophysical effects are seen in the change of the spectral structure of PSD and spectral coherence. The knowledge of these geophysical effects in the long term, are expected to improve decision making capabilities in wind farm optimization algorithms. Additionally, as a potential long-term benefit, these simulations would supposedly provide a better understanding of realistic wind inflow in our simulations, which would help us with better design of Data Assimilation coupling in our LES simulations, as our future computational resource would permit.

VI. Acknowledgements

References

[1]Barthelmie, R. J., Pryor, S. C., Frandsen, S. T., Hansen, K. S., Shepers, J. G., Rados, K., Schlez, W., Neubert, A., Jensen, L. E., and Neckelmann, S., "Quantifying the impact of wind turbine wakes on power output at offshore wind farms," *J. Atmo. Ocean. Technology*, Vol. 27, 2010, pp. 1302–1317.

[2]Barthelmie, R. J. and Jensen, L. E., "Evaluation of power losses due to wind turbine wakes at the Nysted offshore wind farm," *Wind Energy*, Vol. 13, 2010, pp. 573–586.

[3]Porté-Agel, F., Wu, Y.-T., and Conzemius, R. J., "Large-Eddy Simulation of Atmospheric Boundary Layer Flow Through Wind Turbines and Wind Farms," *J. of Wind Eng. and Ind. Aerodynamics*, Vol. 99, 2011, pp. 154–168.

[4]Martinez, L. A., Leonardi, S., Churchfield, M. J., and Moriarty, P. J., "A Comparison of Actuator Disk and Actuator Line Wind Turbine Models and Best Practices for Their Use," AIAA Paper 2012-0900, 2012.

[5]Churchfield, M. J., Lee, S., Moriarty, P. J., Martinez, L. A., Leonardi, S., Vijayakumar, G., and Brasseur, J. G., "A Large-Eddy Simulation of Wind-Plant Aerodynamics," AIAA Paper 2012-0537, 2012.

[6]Chatterjee, T. and Peet, Y., "Actuator Line Wind Turbine Simulations in Atmospheric Turbulent Flows using Spectral Element Method," AIAA paper 2015–0727, 2015, 05 - 9 January 2015, Kissimmmee, Florida.

[7]Chatterjee, T. and Peet, Y., "Large Eddy Simulation of a 3 × 3 wind turbine array using Actuator Line model with spectral elements," AIAA paper 2016–1988, 2016, 04 - 8 January 2016, San Diego, California.

[8]Sorensen, J. N. and Shen, W. Z., "Numerical modelling of Wind Turbine Wakes," *J. Fluids Eng.*, Vol. 124, 2002, pp. 393–399.

[9]Troldborg, N., *Actuator Line Modeling of Wind Turbine Wakes*, Ph.D. thesis, Technical University of Denmark, 2008.

[10]Courtier, P., Thépaut, J. N., and Hollingsworth, A., "A strategy for operational implementation of 4D-Var, using an incremental approach," *Quart. J. Roy. Meteorol. Soc.*, Vol. 120, 1994, pp. 1367–1387.

[11]Auroux, D. and Blum, J., "Back and forth nudging algorithm for data assimilation problems," *C. R. Acad. Sci. Paris*, Vol. 340, 2005, pp. 873–878.

[12]Xia, Q., Lin, C.-L., and Calhoun, R., "Retrieval of urban boundary layer structure from Doppler lidar data. Part I: Accuracy assessment," *J. Atmo. Sci.*, Vol. 65, 2008, pp. 3–20.

[13]Krishnamurthy, R., Choukulkar, A., Calhoun, R. J., Fine, J., Oliver, A., and Barr, K. S., "Coherent Doppler lidar for wind farm characterization," *Wind Energy*, Vol. 16, 2013, pp. 189–206.

[14]Cherukuru, N. W., Calhoun, R. J., Lehner, M., Hoch, S. W., and Whiteman, C. D., "Instrument Configuration for dual-doppler LIDAR Coplanar scans," *J. Appl. Remote Sens.*, Vol. 9, 2015, pp. 096090.

[15]Fischer, P., Lottes, J., Pointer, D., and Siegel, A., "Petascale Algorithms for Reactor Hydrodynamics,," *J. Phys. Conf. Series*, 2008.

[16]Mason, P. J. and Thompson, D. J., "Stochastic backscatter in large-eddy simulations of boundary layers," *J. Fluid. Mech.*, Vol. 242, 1992, pp. 51–78.

[17]Monin, A. S. and Obukhov, A. M., "Basic Laws of Turbulent Mixing in the Ground Layer of the Atmosphere," *Trans. Geophys. Inst. Akad. Nauk. USSR*, Vol. 151, 1954, pp. 163–187.

[18]Calaf, M., Meneveau, C., and Meyers, J., "Large Eddy Simulation Study of Fully Developed Wind-Turbine Array Boundary Layers," *Phys. Fluids*, Vol. 22, 2010, pp. 015110.

[19]Porté-Agel, F., Meneveau, C., and Parlange, M. B., "A scale-dependant dynamic model for large eddy simulation: application to a neutral atmospheric boundary layer," *J. Fluid. Mech.*, Vol. 17, 2000, pp. 261–284.

[20]Deville, M. O., Fischer, P. F., and Mund, E. H., *High-Order Methods for Incompressible Fluid Flow*, Cambridge University Press, Cambridge, UK, 2002.

[21]Chatterjee, T. and Peet, Y. T., "Effect of artificial length scales in Large Eddy Simulation of a neutral atmospheric boundary layer flow: A simple solution to log-layer mismatch," *Physics of Fluids, in review*, 2016.

[22]Bou-Zeid, E., Meneveau, C., and Parlange, M., "A scale-dependant Lagrangian dynamic model for large eddy simulation of complex turbulent flows," *Phys. Fluids*, Vol. 415, 2005, pp. 025125.

[23]Chatterjee, T. and Peet, Y., "Spectra and Large Eddy Structures in the double log-layer in a high Re wind turbine array boundary layer," ASME Turbo Expo GT2016-56359, 2016.

[24]Merrill, B. E., Peet, Y. T., Fischer, P. F., and Lottes, J., "A spectrally accurate method for overlapping grid solution of incompressible Navier-Stokes equations," *J. Comp. Phys.*, Vol. 307, 2016, pp. 60–93.

[25]Krishnamurthy, R., Calhoun, R. J., Fine, J., Billings, B., and Doyle, J. D., "Mesoscale model evaluation with coherent Doppler lidar for wind farm assessment," *Remote Sensing Letters*, Vol. 4, 2013, pp. 579–588.

[26]Magerman, B., "Short-Term Wind Power Forecasts using Doppler Lidar – Masters Thesis," 2014.

[27]Hamilton, N., Kang, H. S., and Cal, C. M. R. B., "Statistical analysis of kinetic energy entrainment in a model wind turbine array boundary layer," *J. Renewable Sustainable Energy*, Vol. 4, 2012, pp. 063105.

[28]Frandsen, S., ans S. Pryor, R. B., Rathmann, O., Larsen, S., Hojstrup, J., and Thogersen, M., "Analytical modelling of wind speed decit in large offshore wind farms," *Wind Energy*, Vol. 9, 2006.

[29]Munters, W., Meneveau, C., and Meyers, J., "Shifted periodic boundary conditions for simulations of wall-bounded flows," *Phys. Fluids.*, Vol. 25, 2016, pp. 025112.